




Article

Phase Stability, Microstructure, and Mechanical Properties of Spark Plasma Sintered Nanocrystalline Boron-Doped AlCoFeMnNi High-Entropy Alloy

S. Pourmohammadi ¹, A. Mohammadnejad ² , A. Bahrami ^{2,*}, S.H. Mousavi Anijdan ³ , N. Park ^{4,5}  and M. Ghosh ⁶

¹ Institute of Materials Science, Technical University of Darmstadt, Alarich-Weiss-Strasse 2, 64287 Darmstadt, Germany; sahar.pourmohammadi@stud.tu-darmstadt.de

² Department of Materials Engineering, Isfahan University of Technology, Isfahan 84156-83111, Iran; a45moham@uwaterloo.ca

³ Department of Mechanical and Industrial Engineering, University of Toronto, Toronto, ON M5S 3G8, Canada; hashem.mousavi@mail.mcgill.ca

⁴ Institute of Materials Technology, Yeungnam University, 280 Daehak-ro, Gyeongsan 38541, Gyeongsangbuk-do, Republic of Korea; nokeun_park@yu.ac.kr

⁵ School of Materials Science and Engineering, Yeungnam University, 280 Daehak-ro, Gyeongsan 38541, Gyeongsangbuk-do, Republic of Korea

⁶ Department of Metallurgy and Materials Engineering, Indian Institute of Engineering Science and Technology, Howrah 711103, India; mghosh.metal@faculty.iests.ac.in

* Correspondence: a.n.bahrami@iut.ac.ir

Abstract: The microstructure and mechanical properties of mechanically alloyed and spark plasma sintered AlCoFeMnNi- x B ($x = 0, 0.5, 1$, and 5 at. %) high-entropy alloys (HEAs) have been investigated. Boron-doped HEAs were synthesized using mechanical alloying up to 50 h of milling. Synthesized powders were then consolidated at 850, 900, and 950 °C for 10 min under a uniaxial pressure of 40 MPa using spark plasma sintering (SPS). A scanning electron microscope, which was equipped with energy dispersive spectroscopy (EDS), together with an optical microscope (OM) were used to analyze the microstructural evolution. X-ray diffraction analysis was used to differentiate the phases formed in the solution. The mechanical properties of the sintered specimens were analyzed using the shear-punch test (SPT). The fracture surface of the SPT samples was studied using SEM. Thermodynamic calculations revealed that by employing this process, it is possible to produce solid solution HEAs with a duplex FCC + BCC structure. It was shown that boron-doped AlCoFeMnNi high-entropy alloys contain some unique attributes. SPS at 900 °C for a sample with boron up to 0.5 at. % leads to the formation of an alloy with the highest shear strength. A further increase in the boron content in the boron-doped HEAs exhibited a decrease in the maximum shear strength. Finally, the correlations between the microstructural and mechanical characteristics of the sintered boron-containing high-entropy alloys are discussed.

Keywords: high-entropy alloy; AlCoFeMnNi; boron; spark plasma sintering; mechanical alloying



Citation: Pourmohammadi, S.; Mohammadnejad, A.; Bahrami, A.; Mousavi Anijdan, S.H.; Park, N.; Ghosh, M. Phase Stability, Microstructure, and Mechanical Properties of Spark Plasma Sintered Nanocrystalline Boron-Doped AlCoFeMnNi High-Entropy Alloy. *Metals* **2023**, *13*, 1025. <https://doi.org/10.3390/met13061025>

Academic Editors: Lin Liu and Tadeusz Kulik

Received: 18 March 2023

Revised: 17 May 2023

Accepted: 22 May 2023

Published: 27 May 2023



Copyright: © 2023 by the authors. Licensee MDPI, Basel, Switzerland. This article is an open access article distributed under the terms and conditions of the Creative Commons Attribution (CC BY) license (<https://creativecommons.org/licenses/by/4.0/>).

1. Introduction

Engineering alloying systems are developed based on the utilization of up to two elements as host elements. Minor amounts of alloying elements are often added to host elements to control the mechanical and physical properties of alloys [1–3]. The concept of alloying was further extended by developing alloying systems using five or more alloying elements in a (near) equimolar ratio. This concept is based on the fact that there is no principal element in the chemistry of the so-called high-entropy alloys (HEAs). This mixing of elements in equimolar ratios creates a high mixing entropy, induces a large lattice strain/distortion, and results in a sluggish diffusion of elements [4–8]. With a proper

selection of elements, HEAs with a simple solid solution structure can be attained [9–12]. HEAs exhibit a unique combination of mechanical properties, i.e., high strength and excellent ductility. Moreover, many reports show that HEAs have promising properties when it comes to corrosion, high-temperature oxidation, and wear [13,14]. HEAs are often synthesized by vacuum arc melting, vacuum induction melting, splat quenching, and sputtering [4]. Vacuum arc melting and other liquid metal production routes are inherently susceptible to solidification defects and structural irregularities. Additionally, when it comes to the casting process, all sorts of problems related to the high temperature oxidation and segregation of alloying elements are expected to come to the fore. Room temperature powder processing routes, and more specifically mechanical alloying, have been suggested as an alternative to liquid-based production methods [15,16]. Mechanical alloying is a widely used powder metallurgy technique with the possibility of controlling the morphologies of powders [17]. More importantly, compared with vacuum melting techniques, mechanical alloying is known to be much cheaper and more cost-effective. Depending on the input energy during the milling, mechanically alloyed powders are often nanocrystalline. Powders synthesized by mechanical alloying can be consolidated using different methods. Amongst different consolidation methods, spark plasma sintering (SPS) has recently gained a lot of attention [15]. SPS has numerous unique characteristics, including relatively quick consolidation time, high density of consolidated components, and minimized high temperature exposure of powders [17]. SPS is essentially carried out under simultaneous application of electric pulse and pressure within a relatively short holding time. Combined mechanical alloying/spark plasma sintering has been successfully applied in synthesizing high-entropy alloys [18]. Even though a lot has been done on the synthesis and characterization of high-entropy alloys, the idea of doping interstitial elements, and more specifically boron, into the matrix of these alloys has not been widely investigated. Supposedly, boron addition results in the formation of new phases in the matrix [19], which are associated with significant enhancements in the hardness and strength [20]. The available literature on the implications and effects of boron doping in high-entropy alloys is very limited. This research is therefore an attempt to investigate the implications of boron addition on the microstructure and mechanical properties of high-entropy alloys. In that regard, this research investigates the phase stability, microstructure, and mechanical properties of mechanically alloyed and spark plasma sintered nanocrystalline boron-doped AlCoFeMnNi high-entropy alloys. The alloy was first synthesized from elemental powders using mechanical milling, followed by consolidation through SPS.

2. Materials and Methods

Briefly, 99.9% purity powders of Fe (with an average particle size of $35\ \mu\text{m} \pm 5$), Al ($23\ \mu\text{m} \pm 5$), Co ($8\ \mu\text{m} \pm 3$), Ni ($3\ \mu\text{m} \pm 1$), Mn ($16\ \mu\text{m} \pm 2$), and B ($1\ \mu\text{m} \pm 0.5$) were purchased (Sigma-Aldrich, Germany). Scanning electron microscope (SEM, Phillips XL30, Eindhoven, The Netherlands) and X-ray diffraction analysis (XRD, $\text{Cu K}\alpha = 1.54\ \text{nm}$) were conducted to investigate the particle size and the chemistry of the powders. Figure 1 shows SEM micrographs of the morphologies of the initial particles, representing the difference in features. It is noticeable in this figure that iron, aluminum, cobalt, and nickel have rather spherical morphologies, while manganese particles show more irregularly shaped morphologies with sharp edges and corners. Figure 2 also depicts the XRD/Energy Dispersive X-ray Spectroscopy (EDS) characteristics of the mixed powders, showing hardly any irregularity in the composition and the phase structure of initial powders. All pure powders, except boron, were mechanically alloyed for about 50 h in a steel vial using steel balls. A ball to powder weight ratio of 10:1, a rotation speed of 350 rpm, and an Ar atmosphere were used for the mechanical alloying. Up to 2 wt. % stearic acid was added to the initial mixture to minimize the sticking of powders with the balls and the container. Afterwards, the powders were sintered at 850, 900, and 950 °C by spark plasma sintering (SPS). The heating and cooling rates were 100 °C/min. Powder samples were held at sintering temperatures for 10 min under a uniaxial pressure of 40 MPa. The diameter and

thickness of the bulk samples were 15 and 1 mm, respectively. The optimum sintering condition was chosen for the sintering of boron-containing samples. To synthesize boron-containing samples, boron was added to the mixture in the last 5 h of milling to obtain four different compositions containing 0, 0.5, 1, and 5 atomic percent of boron. The powders with the $(\text{AlCoFeMnNi})_{100-x}\text{B}_x$ ($x = 0, 0.5, 1$, and 5 at. %) compositions were characterized using SEM and XRD methods to study the microstructural evolution and particle morphologies. Mechanical properties of the bulk samples were assessed using the shear punch test (SPT) with a punch diameter of 3 mm and under the rate of 0.1 mm/s. The fractured surface and the top surface of the specimens were assessed using an SEM and EDS apparatus. Vickers hardness measurements were performed with 30 kg loads. Each hardness experimental point is the average of 5 indents.

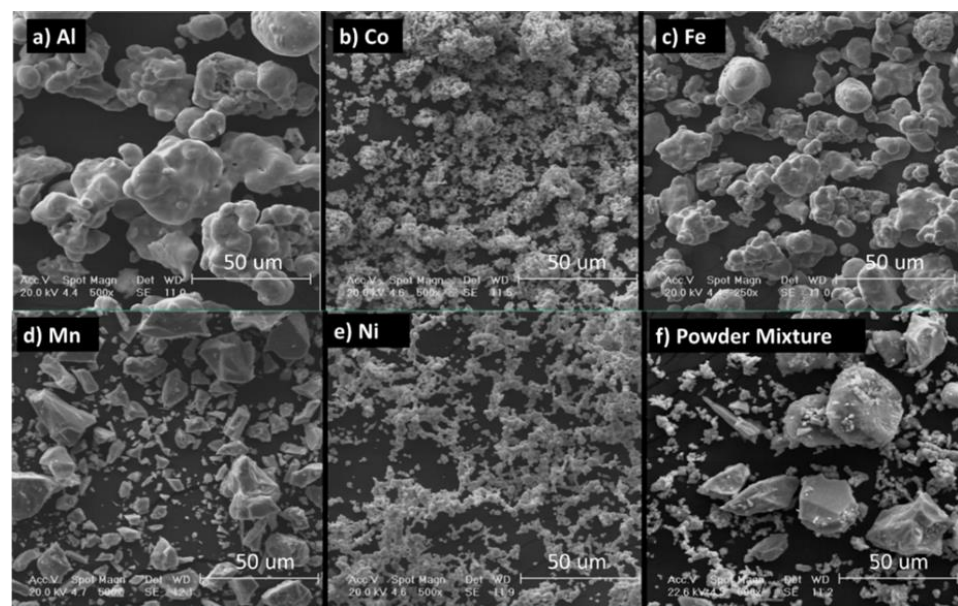


Figure 1. Morphologies of the initial powders: (a) Al, (b) Co, (c) Fe, (d) Mn, (e) Ni, and (f) initial powder mixtures.

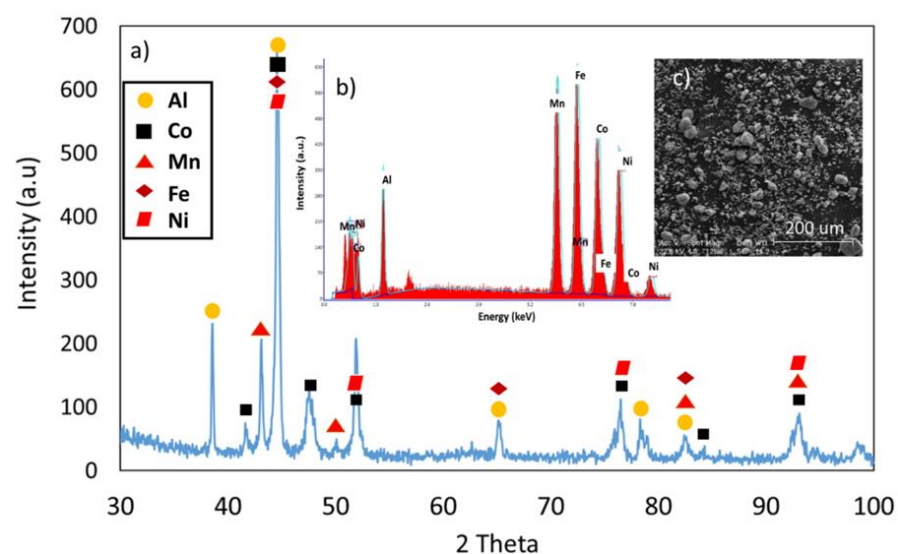


Figure 2. (a) XRD and (b) EDS of the initial powder mixture from the area shown in part (c).

3. Results and Discussion

3.1. Thermodynamic Assessment of Phase Stability and Phase Compositions

The formation of a solid solution in a multi-component alloying system is a function of the difference in the atomic size, electronegativity of components, crystal structure, and the valence number of alloying elements in the alloying system [21–23]. Zhang et al. [24] investigated the effects of these parameters on the formation of different phases in high-entropy alloys. They showed that the formation of FCC, BCC, and FCC+BCC structures in a high-entropy alloy and the stability of a certain crystal structure depend on the difference in the atomic size of the components in the alloying system (δ), the enthalpy of mixing (ΔH_{mix}), and the entropy of mixing (ΔS_{mix}). The latter has the most important ascription to the formation and stability of phases in these alloys. These three parameters can be calculated using the following equations [4]:

$$\delta = 100 \sqrt{\sum_{i=1}^n C_i \left(1 - \frac{r_i}{\bar{r}}\right)^2} \quad (1)$$

$$\Delta H_{\text{mix}} = \sum_{i=1}^n \sum_{j \neq i} \Omega_{ij} C_i C_j \quad (2)$$

$$\Delta S_{\text{mix}} = -R \sum_{i=1}^n C_i \ln C_i \quad (3)$$

in which R is the universal gas constant ($R = 8.314 \text{ J/K}\cdot\text{mol}$); C_i is the molar fraction of element i , $\Omega_{ij} = 4 \Delta_{AB}^{\text{mix}}$; Δ_{AB}^{mix} is the so-called interaction parameter, also known as the enthalpy of mixing in the A-B binary alloy; $\bar{r} = \sum_{i=1}^n C_i r_i$ is the average atomic radius; and r_i is the atomic radius of element i [4]. Zhang et al. [24] concluded that the following conditions should be met to attain a single-phase solid solution in a high-entropy alloying system:

$$\delta \leq 6.6\%, \Delta S_{\text{mix}} \geq 13.38 \text{ J/(K}\cdot\text{mol)}, -15 \text{ KJ/mol} \leq \Delta H_{\text{mix}} \leq 5 \text{ KJ/mol} \quad (4)$$

Further to the aforementioned parameters, another parameter, Ω , was introduced, taking both ΔH_{mix} and ΔS_{mix} into consideration [25,26]. This parameter can be calculated using the next equation:

$$\Omega = |T_m \Delta S_{\text{mix}} / \Delta H_{\text{mix}}| \quad (5)$$

where T_m is the average melting point of the components in the system. T_m is calculated using the below equation:

$$T_m = \sum_{i=1}^n X_i (T_m)_i \quad (6)$$

where $(T_m)_i$ is the melting point of element i in the alloying system. According to this criterion, the solid solution is formed when $\Omega \geq 1.1$, inferring that entropy is expected to be more influential when it comes to the formation of solid solutions [26]. Guo et al. [27] introduced two other parameters: Δx and valence electron count (VEC), with the former being related to the difference between the electronegativity of alloying elements and the latter being related to the density of valence electrons.

$$\Delta x = \sqrt{\sum_{i=1}^n C_i (x_i - \bar{x})^2} \quad (7)$$

$$\text{VEC} = \sum_{i=1}^n (\text{VEC})_i \quad (8)$$

in which $\bar{x} = \sum_{i=1}^n C_i x_i$, where x_i is the Pauling electronegativity of component i in the system and $(\text{VEC})_i$ is the concentration of electrons for the element i in the system. Guo et al. [27] postulated that these parameters cannot be used to evaluate whether a solid solution or an amorphous phase is stable in a multi-component system. VEC is more useful when it comes to the determination of the stability of crystal structures. Based on the proposed criterion, FCC is stable when $\text{VEC} \geq 8$. VEC values lower than 6.87 result in the stabilization of the BCC crystal structure. The physical characteristics of components

in the AlCoFeNiMn alloying system and the enthalpy of mixing for the binary mixtures can be found in the literature [25,27]. Table 1 shows that in this case, the solid solution is stable, there is no indication of the formation of any amorphous or intermetallic phases in this alloying system, and that the final equilibrium microstructure is anticipated to be FCC + BCC.

Table 1. Thermodynamic and phase stability parameters in the AlCoFeMnNi system.

VEC	Δx	Ω	Tm (K)	ΔS_{mix} (J/mol·K)	ΔH_{mix} (kJ/mol·K)	δ (%)	Structure
7.4	0.1473	1.49	1551.86	13.38	−13.92	5.29	FCC + BCC

3.2. Mechanical Alloying and Sintering of the AlCoFeNiMn Alloy

Figure 3 represents an overview of the morphological changes in the powders during milling. The morphology of particles plays a key role in final properties of manufactured parts [28,29]. In the initial powder mixture, different morphologies are visible. As mentioned earlier, larger particles are Mn and Al, while smaller-sized ones are Fe, Co, and Ni. With 10 h of mechanical alloying, larger blocky-shaped particles disappear. They are replaced with smaller-sized particles with flake-like shapes. This clearly shows the amount of plastic deformation during the initial hours of milling. It appears that particles are flattened due to excessive plastic deformation, originating from recurrent high-energy collisions. In addition to the flattening and plastic deformation, some other main reactions, including the cold welding of particles, work hardening of particles, and particle fragmentation, are anticipated to take place. While cold welding enlarges particles, particle fragmentation results in a particle size refinement. Results display that at some point, a balance is reached in the parallel enlargement/refinement reactions. As can be seen in Figure 3, the variations in the mean particle diameters and the morphology of particles are rather marginal after 30 h of mechanical alloying. As reported in one of the current authors' previous works [18], the mean particle size is around 5 μm after 50 h of milling. More importantly, mechanically alloyed samples are mostly spherical with a very narrow size distribution, making these particles suitable for the subsequent sintering process. Spherical powders are expected to have a much better sintering response compared with particles with irregular morphologies [30]. Figure 4 depicts the EDS analysis of the powders after 50 h of milling together with the elemental mapping in the mechanically alloyed sample. There is hardly any deviation from the nominal composition, inferring that milling has been carried out in a well-protected atmosphere. More importantly, all elements are very well-intermingled and the elements are perfectly homogeneously distributed. Both mentioned observations are strong indicators that mechanical alloying has been effectively performed up to 50 h. Inhomogeneity clearly has negative implications for the mechanical properties of engineering alloys [31–33].

Figure 5 represents the XRD spectra of the initial powder mixture, mechanically alloyed AlCoFeNiMn alloy (after 50 h of milling), and sintered specimens (the XRD spectrum of the sample sintered at 850 °C is not reported as it was very similar to that of the sample sintered at 900 °C). Figure 5 shows that sharp peaks, related to different elements, disappear after mechanical milling up to 50 h. It can be seen that 50 h of milling is associated with a complete transformation of elemental powders to a single FCC phase structure. Moreover, mechanical milling has led to a significant decrease in the intensities of XRD peaks and an increase in the peak width, both of which are attributable to the refinement of the crystal structure. A crystallite size as small as 10 nm can be attained after 50 h of milling. As mentioned in one of the current authors' earlier works [18], the final structure of mechanically alloyed powders (single phase FCC or a mixed FCC/BCC) mainly depends on the milling time. At intermediate stages (around 30 h of milling), the alloy has a duplex FCC/BCC structure [18]. With a further increase in the milling time, the ratio BCC/FCC phase content approaches zero in such a way that 50 h milled powders are completely FCC-structured. Sintering at 850 and 900 °C does not change this single-phase structure.

However, XRD peaks become sharper in the sintered samples, inferring that a grain growth has taken place during sintering. Sintering at 950 °C results in the enlargement of crystallite size to 25 nm (calculated by the Wilson equation). Moreover, a BCC phase formed in the structure for the 950 °C sintered sample, in such a way that this alloy has a duplex BCC/FCC phase structure. It appears that the formation of this BCC phase in the structure of the sintered sample is a diffusion-dependent phenomenon. Moreover, the fact that sintering at 850 and 900 °C does not end up in a duplex BCC/FCC structure can be justified by lower diffusion rates at these two temperatures. A 50 °C increase in the sintering is clearly enough to stimulate diffusion and form the BCC phase in the microstructure. The “sluggish diffusion effect” has been a core concept in the development of high-entropy alloy theory from the early stage of its development. It is postulated that the highly distorted lattice of HEAs hinders atomic transport, leading to sluggish atomic movements. This view was supported by the slow kinetic of oxidation and high creep resistance in HEAs. It is also worth mentioning that the diffusion in high-entropy alloys reportedly takes place via the vacancy mechanism. Therefore, it can be concluded that sluggish diffusion is the direct consequence of the comparatively higher enthalpy of vacancy formation in high-entropy alloys as compared with FCC-structured elements. With that said, it can be concluded that the diffusion is highly dependent on temperature. This is a very important issue, as the different nature of the BCC phase, compared with that of the FCC phase, can be used to tailor the mechanical properties. While the BCC phase is often harder (and more brittle), the FCC phase has a higher ductility. To investigate the characteristics and the nature of phases, SEM/EDS analyses were conducted on the sintered specimens.

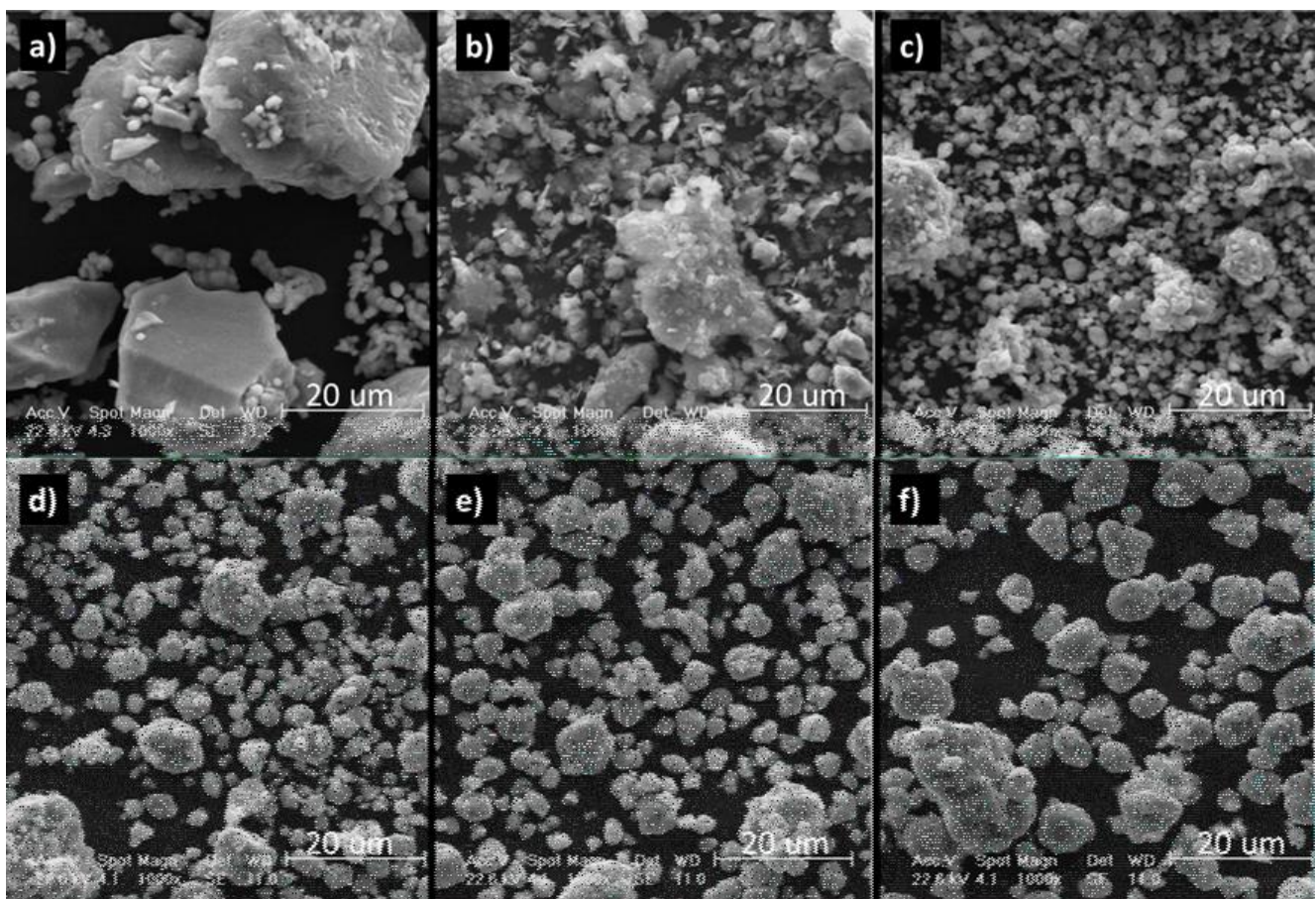


Figure 3. Variations in the morphology of (a) initial powders after (b) 10, (c) 20, (d) 30, (e) 40, and (f) 50 h of milling.

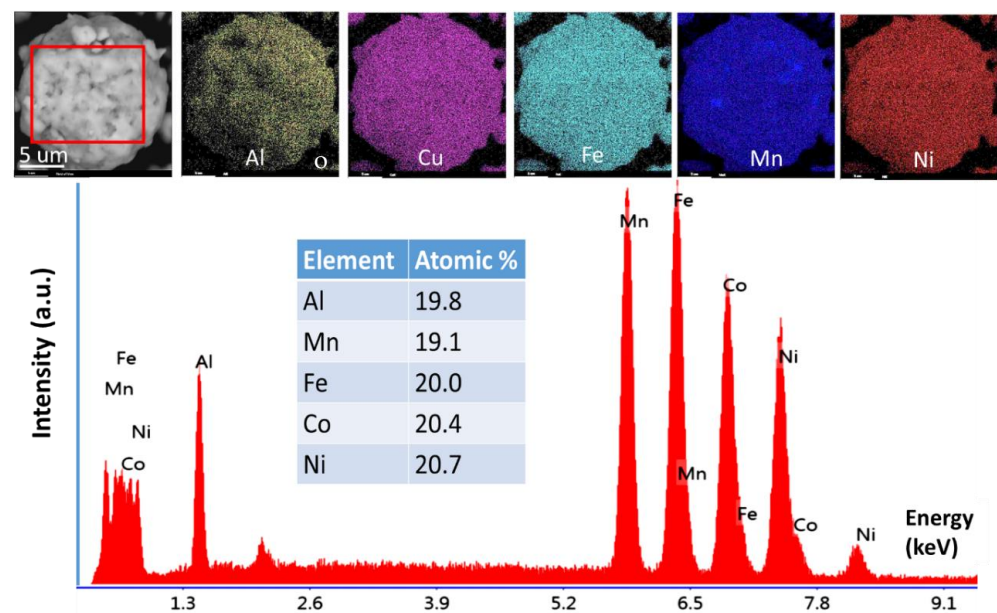


Figure 4. EDS analysis and elemental mapping 50 h milled powder sample.

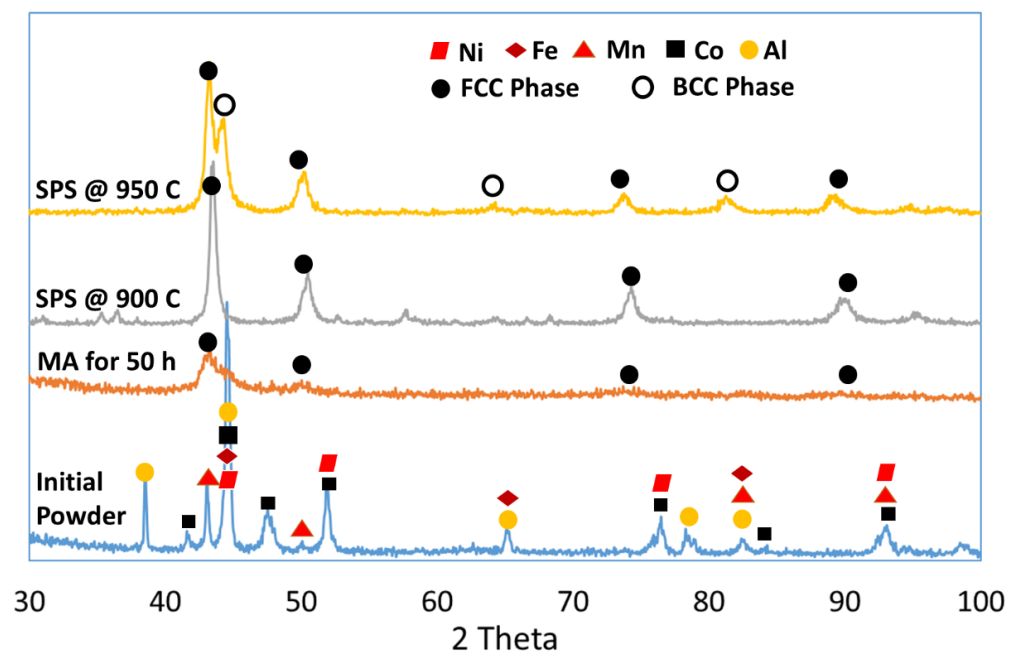


Figure 5. XRD analyses of the initial powders and mechanically alloyed powders for 50 h, sintered at 900 and 950 °C.

SEM/EDS analyses of the sample, sintered at 950 °C, are depicted in Figure 6. There are several interesting features in this figure. Firstly, the porosities can be divided into two distinct size groups. The first category consists of very small porosities that are locked inside grain interiors. The second category is for the large-sized porosities that are positioned between the particle spaces as well as in the triple junctions. It is important to mention that two types of phases are present in the structure. They include the dominant greyish phase and a secondary white phase, dispersed in the particles spacing. It is worth mentioning that in some locations, the white phase is in the form of a continuous film over the matrix greyish phase. Seemingly, sintering at 950 °C led to the re-distribution of alloying elements into the mentioned phases. It also led to the formation of a duplex FCC/BCC structure, as predicted using thermodynamic calculations and confirmed with XRD results. Analyzing

the SEM micrograph using an image analyzer software (Image-J), we revealed that the white phase is about 10% of the whole microstructure. In addition, EDS point analysis was conducted on these two phases (the spots are depicted in Figure 6). The results of EDS analyses of the white and the greyish areas are shown in Figure 6. The EDS analysis shows a substantial depletion of Ni and Al elements at the grain boundaries for the white phase. The atomic percentages of Ni and Al are 17 and 16%, respectively, in the white phase. These values are well below the nominal alloy composition (i.e., 20% for these elements). Moreover, the EDS analysis of the greyish phase depicts that the depleted Ni and Al diffused away from the grain boundaries within the greyish phase. On the one hand, the results imply that Fe and Co have segregated into the white phase at the grain boundaries. However, it is seen that Mn did not show any tendency for segregation into either of the two mentioned phases. Since both Ni and Al have FCC structures, the greyish phase is possibly an FCC phase. The white phase is possibly the BCC phase due to the BCC structure of the Fe element. This corroborates with the XRD results, pointing out the dominance of an FCC phase in the structure.

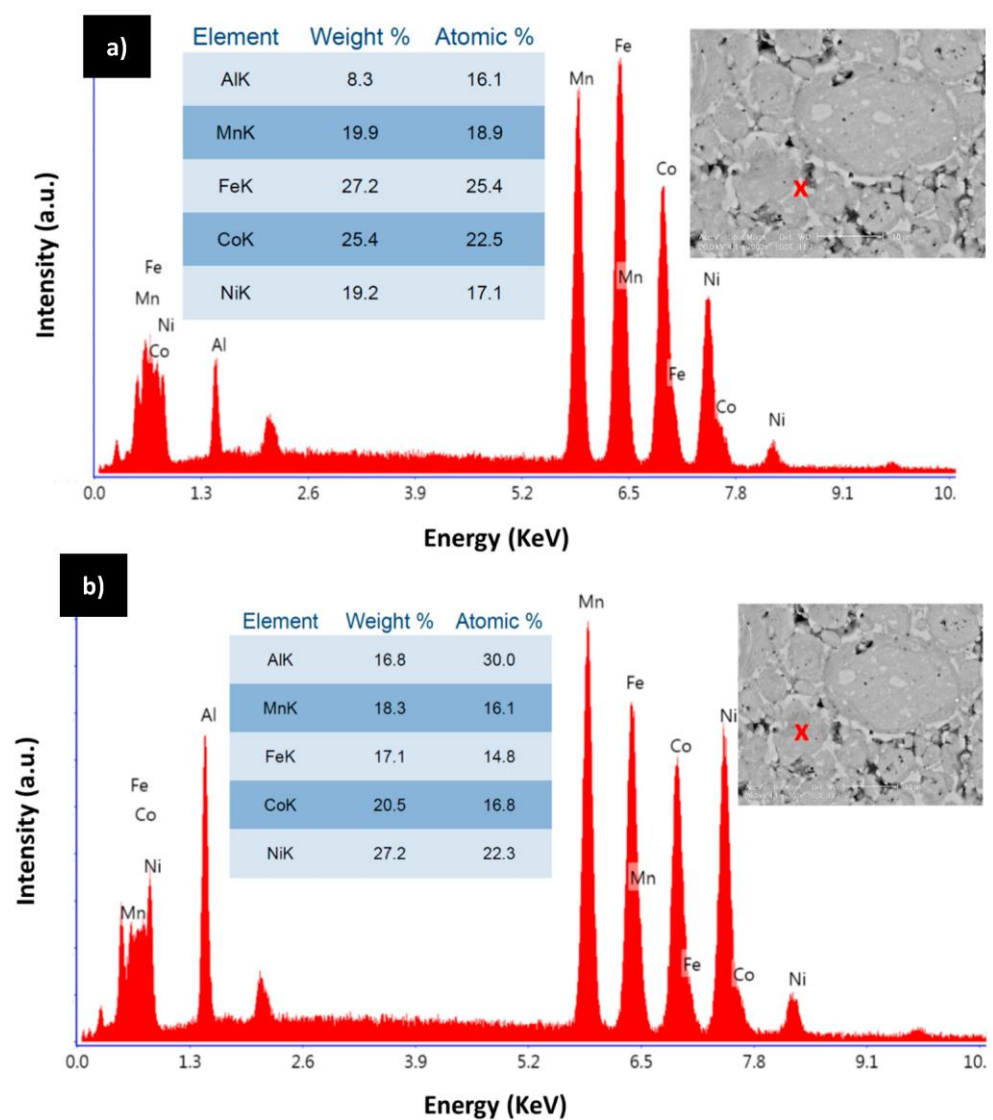


Figure 6. EDS analyses of the (a) white and (b) greyish phases in the sample, sintered at 950 °C.

Figure 7 depicts the shear test results as well as fracture surfaces of the samples, sintered at 850, 900, and 950 °C. Results show that the highest shear strength is achieved in the sample sintered at 900 °C. It appears that the strength is controlled by both the porosity

percentage and the BCC/FCC compositions. As previously mentioned [18], the porosity in this system varies from 2 to 7%, depending on the sintering temperature. The lower the sintering temperature, the higher the porosity percentage. In addition, it is not surprising that the fracture in the 850 °C sintered sample is controlled by porosities (as highlighted in Figure 7b). The increasing sintering temperature is associated with a decrease in the porosity contents, and this in turn is associated with an improvement in maximum shear strength to values as high as 170 MPa. A further increase in the sintering temperature up to 950 °C results in a decrease in the maximum shear strength down to 100 MPa. This can be justified with the fact that sintering at 950 °C leads to the precipitation of the less ductile BCC phase (as discussed earlier).

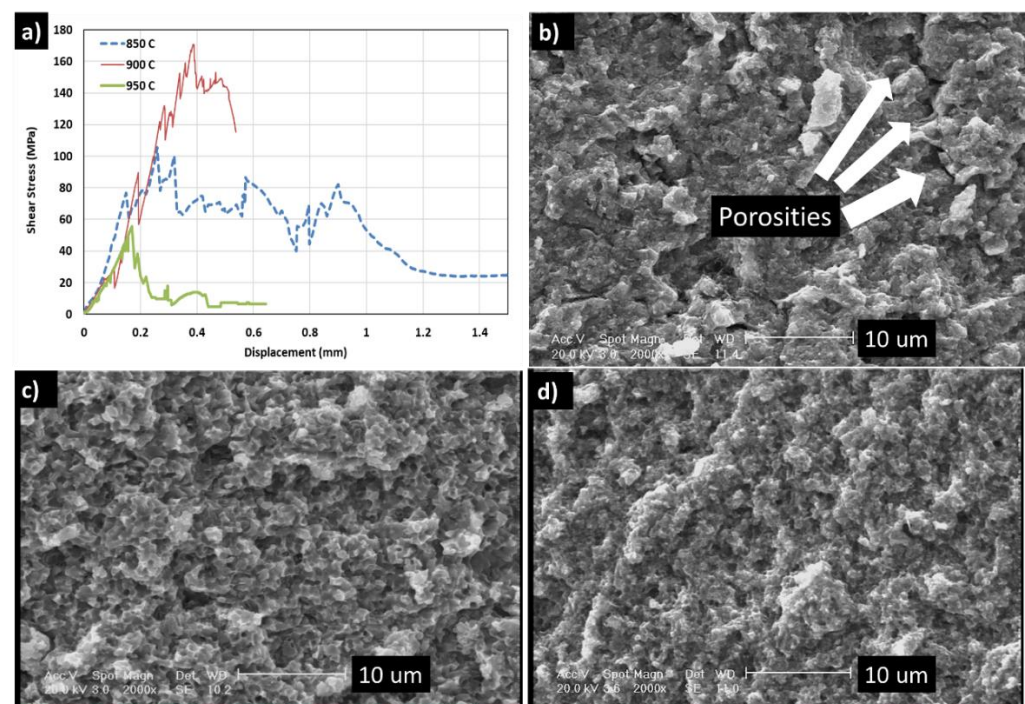


Figure 7. Results of (a) shear test and fracture surfaces of samples sintered at (b) 850, (c) 900, and (d) 950 °C.

3.3. Mechanical Alloying and SPS of the AlCoFeNiMn- x B ($x = 0, 0.5, 1$, and 5 at. %) Alloy

The SEM images of the milled boron-containing samples (Figure 8) show proper milling with the occurrence of further refinement of the quasi-spherical shaped particles as the boron content increases, compared with the core HEA. A slight reduction in the average particle diameter and the size distribution of the powders can be observed with increasing the boron content. The particle size of the powder reduces to about 1–2 µm in HEA containing 5 at.% boron. Figure 9 shows XRD spectra of 50 h milled boron-containing specimens. As mentioned earlier, the microstructure of a 50 h milled sample is predominantly FCC. Boron doping up to 1% does not change the FCC structure of the milled alloys. The only noticeable effect of boron doping on the microstructure of the base HEA is the implications of boron for the crystallite size of the milled samples. In fact, boron significantly decreases crystallite size to values less than 10 nm. This can be inferred from peak broadening and a considerable decrease in the intensity of XRD peaks. Further increase in the boron content by up to 5% is associated with the formation of the FCC/BCC duplex structure. The 50 h milled 5% boron-containing specimen has a clearly different XRD spectrum compared with that of other samples. Given that boron doping increases the diffusion rate of alloying elements [15], and providing that the formation of the BCC phase was postulated to be a diffusional reaction, this observation can be justified.

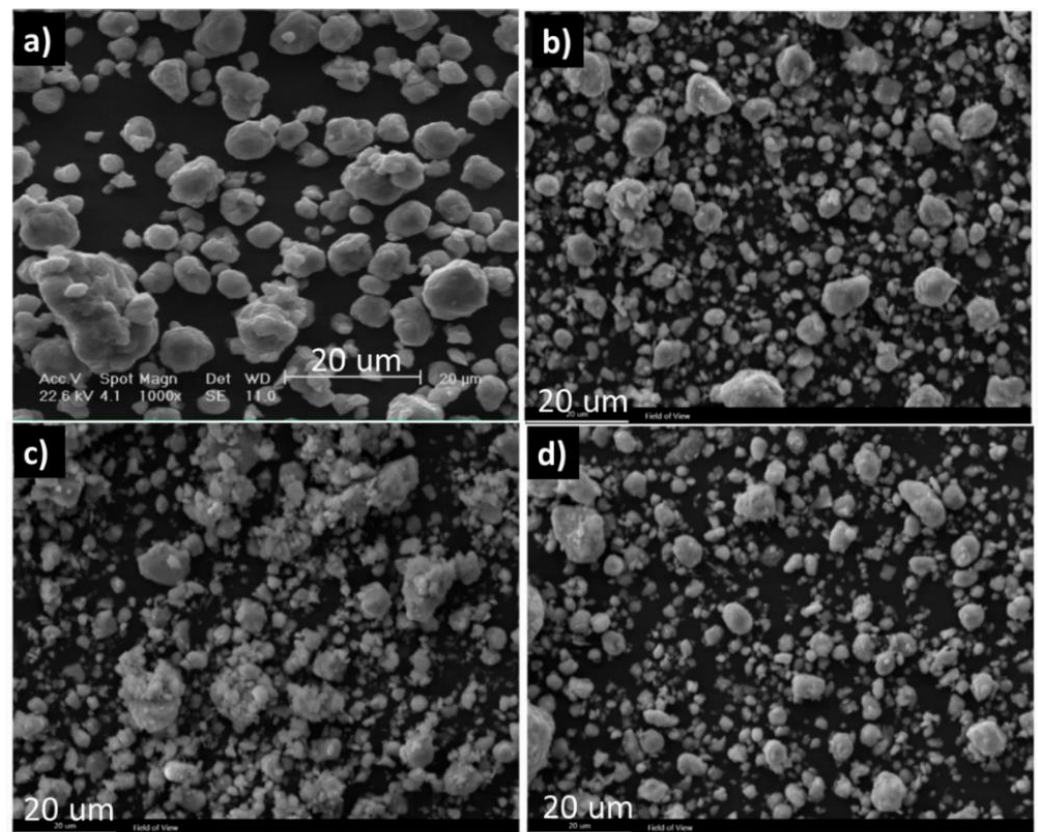


Figure 8. SEM micrographs of mechanically alloyed powders, containing (a) 0, (b) 0.5, (c) 1, and (d) 5% boron.

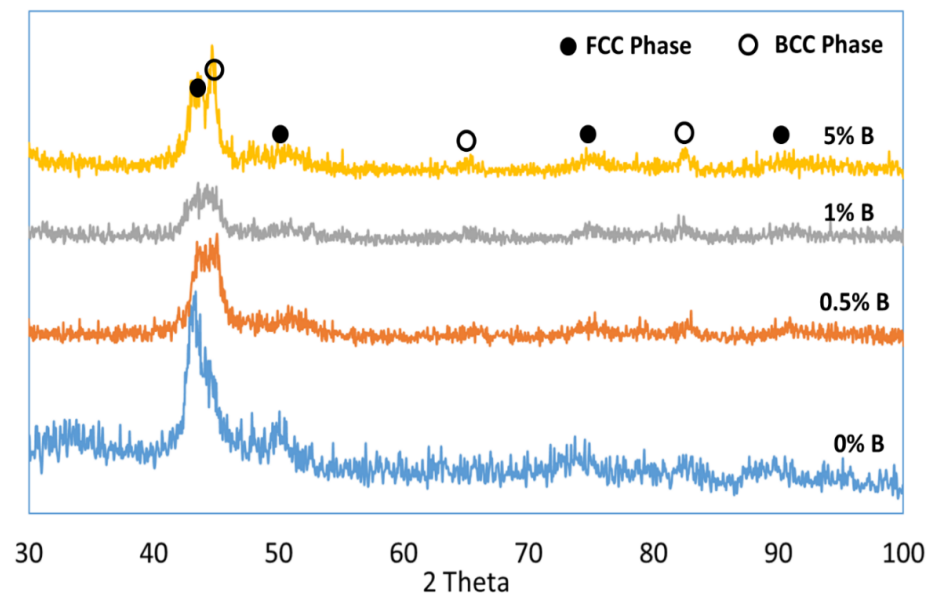


Figure 9. Variation in XRD spectra of 50 h milled samples with boron content.

To explore the impact of B on the sintering of the fundamental HEA, samples that contained boron were subjected to sintering at a temperature of 900 °C. The selection of this temperature was guided by the previous results and shear test outcomes for the base alloy. Figure 10a shows the effects of boron addition on the porosity content of sintered alloys. Figure 10b shows how sintering temperature can change the porosity percentage of the base alloy. Based on these images, one can conclude that an increase

in the sintering temperature is associated with a decrease in the porosity percentage of the sintered specimens. Boron addition significantly affects the porosity percentage of the sintered specimens. Moreover, B appears to enhance the diffusion and mobility of alloying elements during high-temperature sintering. In fact, boron is expected to distort the lattice structure and provide faster diffusion paths for the movement and diffusion of alloying elements. Figure 11 depicts the effects of sintering on the XRD spectra of the AlCoFeNiMn-1%B and AlCoFeNiMn-5%B alloys. XRD spectra of these alloys are shown as typical XRD of low and high B-containing alloys. In both cases, sintering significantly increases the crystallite size. This is confirmed by the observed sharp increase in the intensity of the XRD peaks. In that regard, peak broadening is an indication of decreasing crystallite size. This is not surprising, as thermal exposure during sintering provides an appropriate condition for the grain boundaries' movement.

Figure 12 depicts the elemental mapping of the sintered AlCoFeNiMn-5%B alloy. As expected, the sintered alloy, in this case, has a duplex structure, which is essentially the distribution of a white BCC phase in an FCC matrix. The BCC phase has a noticeably lower aluminum content, inferring that aluminum has been depleted from this phase during sintering. Another observation worth mentioning is the low porosity percentage in the sintered sample, which is attributable to the presence of boron in the structure.

Figure 13 shows the shear test behavior of boron-containing samples compared with that of the base alloy. SEM micrographs in this image show the distribution of the white BCC phase in the matrix, which is related to the AlCoFeNiMn-0.5%B and AlCoFeNiMn-5%B alloys. Shear test results indicate that boron addition up to 0.5% significantly enhances maximum shear strength. Further boron addition is associated with the deterioration of mechanical properties. It appears that boron content influences the shear strength by decreasing the porosity contents of sintered alloys on the one hand and increasing BCC phase percentage on the other hand. While a reduced porosity concentration clearly has positive implications for the mechanical properties, the presence of a coarse and brittle BCC structure negatively affects mechanical properties. Finally, it is clear that 0.5% B creates an optimum condition. The comparison of the hardness of the HEA sample with that of the optimum sample (0.5% B) shows an increase from 500 to 580 VHN, which is in accordance with the shear test data.

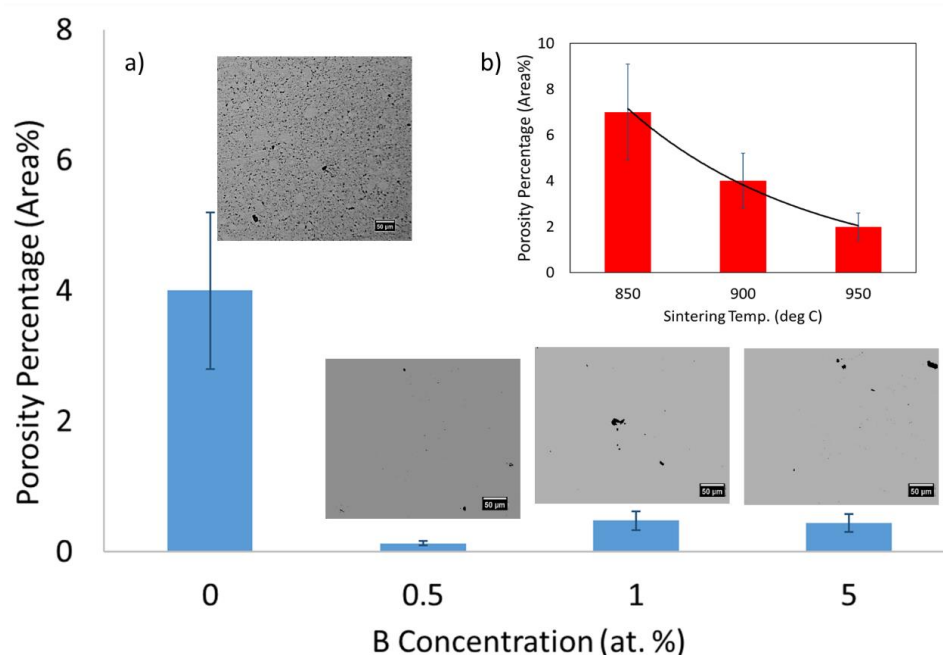


Figure 10. Variation in porosity percentages in the sintered specimens with (a) boron content and (b) sintering temperature (in the base alloy).

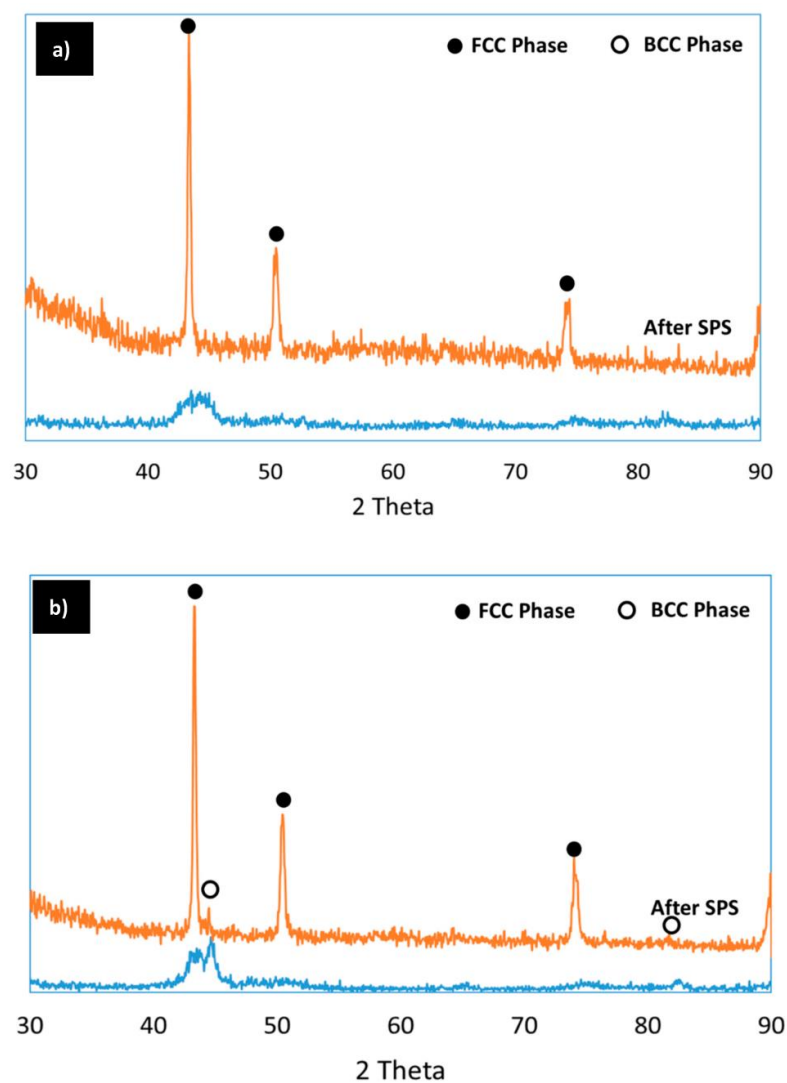


Figure 11. Effects of sintering on the XRD spectra of (a) AlCoFeNiMn-1%B and (b) AlCoFeNiMn-5%B alloys.

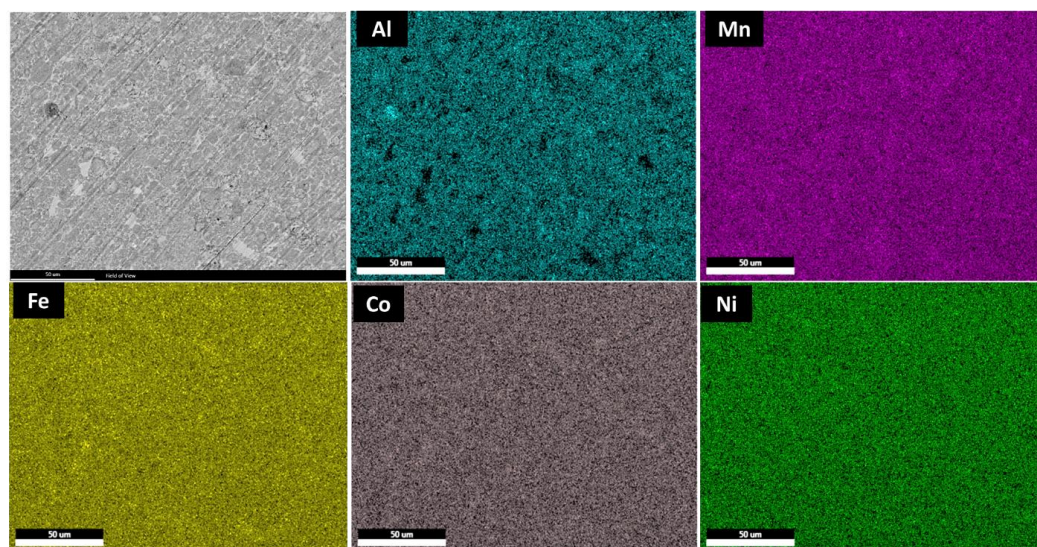


Figure 12. Elemental mapping in sintered AlCoFeNiMn-5%B alloy.

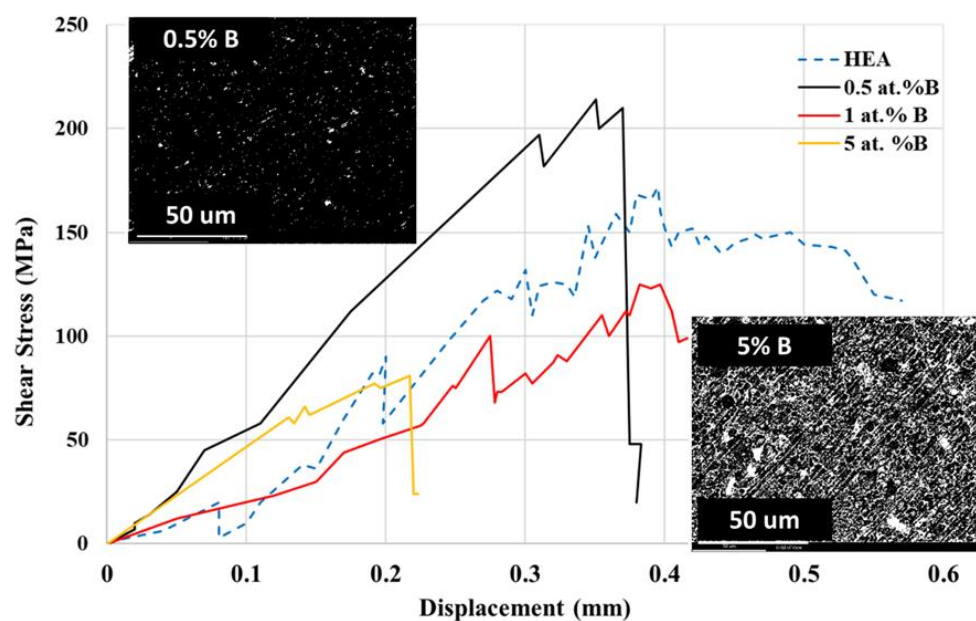


Figure 13. Effect of boron concentration on the shear strength of the sintered HEAs.

4. Conclusions

This study was conducted to investigate the properties of the boron-doped AlCoFeMnNi high-entropy alloy. The alloy was perfectly synthesized using the mechanical alloying method, resulting in a single FCC or a duplex FCC/BCC microstructure. Thermodynamic calculations showed that the alloy is expected to have a duplex FCC/BCC microstructure. However, it appears that the appearance of the BCC phase in the microstructure is a diffusional process. It is also noteworthy that an increase in the sintering temperature elevates the likelihood of BCC phase formation. The addition of B to the base alloy has two notable implications. Firstly, the inclusion of boron significantly enhances the sintered quality of the components, specifically in terms of the concentration of porosities in the sintered sample. Secondly, B promotes the formation of the BCC phase, and the greater the B concentration, the greater the BCC phase content within the final microstructure is. The mechanical properties of the sintered specimens are influenced by the interplay of the mentioned parameters. While the reduction in the porosity is expected to positively affect the mechanical properties of the sintered specimens, the increase in the BCC phase-volume fraction adversely influences mechanical properties. In this investigation, 0.5 at.% boron addition was found to be the optimum addition.

Author Contributions: S.P.: Data curation; Formal analysis; Investigation; Writing. A.M.: Methodology; Writing. A.B.: Supervision; Methodology; Writing—review and editing. S.H.M.A.: Supervision; Methodology. N.P.: Supervision; Writing—review and editing. M.G.: Supervision; Writing—review and editing. All authors have read and agreed to the published version of the manuscript.

Funding: This research received no external funding.

Institutional Review Board Statement: Not applicable.

Informed Consent Statement: Not applicable.

Data Availability Statement: Not applicable.

Acknowledgments: The authors wish to offer their thanks and appreciation to Isfahan University of Technology for the support and involvement during this study.

Conflicts of Interest: The authors declare that they have no conflicts of interest.

References

1. Zhang, L.; Xiong, D.; Su, Z.; Li, J.; Yin, L.; Yao, Z.; Wang, G.; Zhang, L.; Zhang, H. Molecular dynamics simulation and experimental study of tin growth in SAC lead-free microsoldier joints under thermo-mechanical-electrical coupling. *Mater. Today Commun.* **2022**, *33*, 104301. [\[CrossRef\]](#)
2. Gao, Q.; Ding, Z.; Liao, W. Effective elastic properties of irregular auxetic structures. *Compos. Struct.* **2022**, *287*, 115269. [\[CrossRef\]](#)
3. Zhang, Z.; Yang, Q.; Yu, Z.; Wang, H.; Zhang, T. Influence of Y₂O₃ addition on the microstructure of TiC reinforced Ti-based composite coating prepared by laser cladding. *Mater. Charact.* **2022**, *189*, 111962. [\[CrossRef\]](#)
4. Zhang, Y.; Zuo, T.T.; Tang, Z.; Gao, M.C.; Dahmen, K.A.; Liaw, P.K.; Lu, Z.P. Microstructures and properties of high-entropy alloys. *Prog. Mater. Sci.* **2014**, *61*, 1–93. [\[CrossRef\]](#)
5. Tsai, K.Y.; Tsai, M.H.; Yeh, J.W. Sluggish diffusion in Co–Cr–Fe–Mn–Ni high-entropy alloys. *Acta Mater.* **2013**, *61*, 4887–4897. [\[CrossRef\]](#)
6. Zhang, P.; Wang, S.; Lin, Z.; Yue, X.; Gao, Y.; Zhang, S.; Yang, H. Investigation on the mechanism of micro-milling CoCrFeNiAlX high entropy alloys with end milling cutters. *Vacuum* **2023**, *211*, 111939. [\[CrossRef\]](#)
7. Hung, P.K.; Yeh, J.W.; Shun, T.T.; Chen, S.K. Multi-principal-element alloys with improved oxidation and wear resistance for thermal spray coating. *Adv. Eng. Mater.* **2004**, *6*, 74–78. [\[CrossRef\]](#)
8. He, H.; Wang, J.; Cao, Y.; Yang, X.; Zhao, G.; Yang, W.; Fang, J. Effect of Re and C on mechanical properties of NbTaW0.4 refractory medium-entropy alloy at elevated temperature. *J. Alloy. Compd.* **2023**, *931*, 167421. [\[CrossRef\]](#)
9. Cantor, B.; Chang, I.T.H.; Knight, P.; Vincent, A.J.B. Microstructural development in equiatomic multicomponent alloys. *Mater. Sci. Eng. A* **2004**, *375–377*, 213–218. [\[CrossRef\]](#)
10. Miracle, D.B.; Senkov, O.N. A critical review of high entropy alloys and related concepts. *Acta Mater.* **2017**, *122*, 448–511. [\[CrossRef\]](#)
11. Yeh, J.W. Recent Progress in High Entropy Alloys. *Ann. Chem. Sci. Mat.* **2006**, *31*, 633–648. [\[CrossRef\]](#)
12. Miracle, D.B.; Miller, J.D.; Senkov, O.N.; Woodward, C.; Uchic, M.D.; Tiley, J. Exploration and development of high entropy alloys for structural applications. *Entropy* **2014**, *16*, 494. [\[CrossRef\]](#)
13. Wu, J.M.; Lin, S.J.; Yeh, J.W.; Chen, S.K. Adhesive wear behavior of Al_xCoCrCuFeNi high-entropy alloys as a function of aluminum content. *Wear* **2006**, *261*, 513–519. [\[CrossRef\]](#)
14. Chou, Y.L.; Wang, Y.C.; Yeh, J.W.; Shih, H.C. Pitting corrosion of the high-entropy alloy Co_{1.5}CrFeNi_{1.5}Ti_{0.5}Mo_{0.1} in chloride-containing sulphate solutions. *Corros. Sci.* **2010**, *52*, 3481–3491. [\[CrossRef\]](#)
15. Mohammadnejad, A.; Bahrami, A.; Sajadi, M.; Karimi, P.; Fozveh, H.R.; Mehr, M.Y. Microstructure and mechanical properties of spark plasma sintered nanocrystalline Ni₃Al-xB (0.0 < x < 1.5 at%) Alloy. *Mater. Today Commun.* **2017**, *17*, 161–168.
16. Mohammadnejad, A.; Bahrami, A.; Sajadi, M.; Mehr, M.Y. Spark plasma sintering of Ni₃Al-xB-1wt% CNT (0.0 < x < 1.5 at%) nanocomposite. *J. Alloys Comp.* **2019**, *788*, 461–467.
17. Mardiha, P.; Bahrami, A.; Mohammadnejad, A. Towards a high strength ductile Ni/Ni₃Al/Ni multilayer composite using spark plasma sintering. *Sci. Sinter.* **2019**, *51*, 401–408. [\[CrossRef\]](#)
18. Bahrami, A.; Mohammadnejad, A.; Sajadi, M. Microstructure and mechanical properties of spark plasma sintered AlCoFeMnNi high entropy alloy (HEA)-carbon nanotube (CNT) nanocomposite. *J. Alloys Comp.* **2021**, *862*, 158577. [\[CrossRef\]](#)
19. Liu, X.; Lei, W.; Ma, L.; Liu, J.; Liu, J.; Cui, J. Effect of Boron on the microstructure, phase assemblage and wear properties of Al_{0.5}CoCrCuFeNi high-entropy alloy. *Rare Met. Mater. Eng.* **2016**, *45*, 2201–2207.
20. Seol, J.B.; Bae, J.W.; Li, Z.; Han, J.C.; Kim, J.G.; Raabe, D.; Kim, H.S. Boron doped ultra-strong and ductile high-entropy alloys. *Acta Mater.* **2018**, *151*, 366–376. [\[CrossRef\]](#)
21. Zhang, H.; Xiao, Y.; Xu, Z.; Yang, M.; Zhang, L.; Yin, L.; Chai, S.; Wang, G.; Zhang, L.; Cai, X. Effects of Ni-decorated reduced graphene oxide nanosheets on the microstructural evolution and mechanical properties of Sn-3.0Ag-0.5Cu composite solders. *Intermetallics* **2022**, *150*, 107683. [\[CrossRef\]](#)
22. Chen, Y.; Sun, S.; Zhang, T.; Zhou, X.; Li, S. Effects of post-weld heat treatment on the microstructure and mechanical properties of laser-welded NiTi/304SS joint with Ni filler. *Mater. Sci. Eng. A* **2020**, *771*, 138545. [\[CrossRef\]](#)
23. Yuhua, C.; Yuqing, M.; Weiwei, L.; Peng, H. Investigation of welding crack in micro laser welded NiTiNb shape memory alloy and Ti6Al4V alloy dissimilar metals joints. *Opt. Laser Tech.* **2017**, *91*, 197–202. [\[CrossRef\]](#)
24. Zhang, C.H.; Zhang, F.; Shuanglin, C.H.; Weisheng, C. Computational thermodynamics aided high-entropy alloy design. *J. Metals* **2012**, *64*, 839–845. [\[CrossRef\]](#)
25. Zhang, Y.; Zhou, Y. Solid solution criteria for high entropy alloys. *Mater. Sci. Forum* **2007**, *561–565*, 1337–1339. [\[CrossRef\]](#)
26. Sheng, G.; Liu, C.T. Phase stability in high entropy alloys: Formation of solid solution phase or amorphous phase. *Progress Nat. Sci. Mater. Int.* **2011**, *21*, 433–446.
27. Guo, S.; Ng, C.; Lu, J.; Liu, C.T. Effect of valence electron concentration on stability of fcc or bcc phase in high entropy alloys. *J. Appl. Phys.* **2011**, *109*, 103505–1–103505–5. [\[CrossRef\]](#)
28. Niu, X.; Zhu, S.; He, J.; Liao, D.; Correia, J.A.F.O.; Berto, F.; Wang, Q. Defect tolerant fatigue assessment of AM materials: Size effect and probabilistic prospects. *Int. J. Fatigue* **2022**, *160*, 106884. [\[CrossRef\]](#)
29. Chen, W.; Fu, Z.; Fang, S.; Xiao, H.; Zhu, D. Alloying behavior, microstructure and mechanical properties in a FeNiCrCo_{0.3}Al_{0.7} high entropy alloy. *Mater. Des.* **2013**, *51*, 854–860. [\[CrossRef\]](#)

30. Khouzani, M.K.; Bahrami, A.; Mehr, M.Y. Spark plasma sintering of Stellite[®]-6 superalloy. *J. Alloys Comp.* **2019**, *782*, 461–468. [[CrossRef](#)]
31. Fang, J.X.; Wang, J.X.; Wang, Y.J.; He, H.T.; Zhang, D.B.; Cao, Y. Microstructure evolution and deformation behavior during stretching of a compositionally inhomogeneous TWIP-TRIP cantor-like alloy by laser powder deposition. *Mater. Sci. Eng. A* **2022**, *847*, 143319. [[CrossRef](#)]
32. Zhu, Q.; Chen, J.; Gou, G.; Chen, H.; Li, P. Ameliorated longitudinal critically refracted—Attenuation velocity method for welding residual stress measurement. *J. Mater. Proc. Tech.* **2017**, *246*, 267–275. [[CrossRef](#)]
33. Zhang, B.; Wang, Z.; Yu, H.; Ning, Y. Microstructural origin and control mechanism of the mixed grain structure in Ni-based superalloys. *J. Alloy. Compd.* **2022**, *900*, 163515. [[CrossRef](#)]

Disclaimer/Publisher’s Note: The statements, opinions and data contained in all publications are solely those of the individual author(s) and contributor(s) and not of MDPI and/or the editor(s). MDPI and/or the editor(s) disclaim responsibility for any injury to people or property resulting from any ideas, methods, instructions or products referred to in the content.